

STIMULATION OF SPARK-PLASMA SINTERING OF MIXTURES OF OXIDE–NON-OXIDE COMPONENTS BY ADDING A SOLID SOLUTION TaB₂–NbC AND THROUGH A NICKEL MELT IN MIXTURES OF METAL POWDERS

A. V. Hmelov^{1,2}

Translated from *Novye Ogneupory*, No. 2, pp. 14 – 29, February, 2021.

Original article submitted January 4, 2021.

The effects of mixtures of Ni–Ta and Ni–Zr powders combined with sintered solid solution TaB₂–NbC during spark-plasma sintering of compositions at a pressing loading of 60 MPa in the range 1200 – 1600°C on the phase composition, percent content of Ti, Ta, and Zr in the sialon; microstructure; grain sizes of crystalline phases; relative density; linear shrinkage; physical-mechanical properties; linear correlation of the elasticity modulus and fracture toughness of mullite–β–SiAlON–TiC and mullite–β–SiAlON–*c*-ZrO₂ samples are shown. Synthesized powders of β–SiAlON and TiC are characterized by extensive crystallization of β–SiAlON and TiC. *c*-ZrO₂ spark-plasma sintered at 1400°C and solid solution TaB₂–NbC, at 1800°C, show extensive crystallization of *c*-ZrO₂ and (Nb,Ta)C, B, and Ni(Nb,Ta); and varying crystallization of NiTi, NiTa, NiZr, and NiZr₂ phases in the range 1200 – 1600°C. The microstructures of ceramic phases of samples with Ta additive are more uniformly and densely sintered. Particles of NiTi and NiTa in samples with Ta additive are uniformly and densely packed, unlike particles of NiTi, NiZr and NiZr₂ in samples with Zr additive. Sintering of compositions with Ta additive proceeds uniformly and extensively with formation of polydisperse compositions of crystalline phase grains. Samples with Ta additive show active growth and larger values of physical-mechanical properties, higher crack resistance, and better linear correlation of elasticity modulus and fracture toughness in the range 1200 – 1600°C.

Keywords: mullite–β–SiAlON–TiC; mullite–β–SiAlON–*c*-ZrO₂; solid solution TaB₂–NbC; mixtures of Ni–Ta and Ni–Zr powders, spark-plasma sintering; properties.

Spark-plasma sintering of solids with added powders of metals or their mixtures is the main method for producing solid and impact-resistant ceramics and cermets [1 – 5]. The nonuniform evolution of this sintering affects the phase composition and microstructure of boundary layers of oxide–oxide-free and oxide–oxide-free–metal crystalline phases and, as a result, causes variations in the elasticity modulus, fracture toughness, and hardness of these materials [2 – 5]. The degree of crystallinity, brittleness or density of crystalline

phases, homogeneity of the microstructure, and width and ratio of brittle and elastic properties of boundary layers are responsible for the relationship between the phase composition, microstructure, and properties of the boundary layers of crystalline phases [2 – 5]. Less dense crystalline phases, in particular *h*-BN, β-WC, β-WB, and β-Zr, Ta, form nonuniform, broad, and brittle intermediate layers while amorphous carbon is extensively incorporated and accumulated between grains. As a result, the plastic properties of these boundary layers are degraded; regions of dislocations, microcracks, and boundary layers are generated; and the boundary structure of the material grains becomes brittle [2, 3, 5]. Dense crystalline phases, e.g., *c*-BN, β-MoC, β-MoB, and β-Ta, Zr,

¹ Riga Technical University, Institute of Silicate Materials, Riga, Latvia.

² aleksejs.hmelov44@gmail.com

form uniform, narrow, and strong boundary layers that promote uniform and complete distribution of the plastic properties and propagation of microcracks along a tortuous trajectory at slow speed or hinder the advance of microcracks in boundary layers, as a result of which the boundary structure of the material grains densifies and strengthens [2–5]. These properties of the boundary layers are important because they determine how extensively and evenly ceramic and cermet materials absorb, accumulate, and dissipate impact energy and the ratio of absorption and dissipation/accumulation of different amounts of impact energy [2–5].

A method in which *c*-ZrO₂ or solid solution TiC–ZrC is added to spark-plasma sintered ceramic and cermet compositions to densify and strengthen the boundary grain structure has been used [6–8]. Such additives have low efficiencies because they have dense structures and cause nonuniform and incomplete solid-state diffusion at the boundaries of the grains being sintered [6–8]. Also, the densification and strengthening of the grain boundary structure with added solid solution TiC–ZrC depends considerably on the structure and percent content of an actual component in this solid solution [7, 8].

A method for densification and strengthening the grain boundary structure by producing solid solution ZrB₂–TaSi₂ during spark-plasma sintering of the ceramic composition ZrB₂–SiC–TaSi₂ is known [9]. The sintering evolves and the solid solution forms simultaneously, which facilitates more extensive and complete incorporation of the solid-solution crystalline phase into the grain boundary structure to form uniform and narrow boundary layers between oxide-free crystalline phases and solid solutions in addition to dense intermediate layers between solid-solution crystalline phases [9]. This mechanism of densification and strengthening of the grain boundary structure is realized through solid-state sintering and depends on the structure and percent content of an actual component in the solid solution [9].

Another method for densification and strengthening of the grain boundary structure relates to spark-plasma sintering of cermet compositions using a nickel melt with added molybdenum powder [10–12]. As a result, diffusion through the formed low-melting eutectic is accelerated and evenly

evolved to produce solid solutions of cermet and metallic phases of various compositions and stoichiometries [10–12]. The percent ratio of Ni and Mo in the sintered cermet compositions is important and determines the type, mechanism, and rate of sintering and the extent of side processes, in particular recrystallization and coalescence of particles of solid solutions of cermet and metallic phases [10–12]. Embrittlement (crumbling) to form microcracks occurs or the material grain boundary structure densifies and strengthens depending on the sintering specifics [10–12].

The goal of the present work was to study the effect of mixtures of Ni, Ta and Ni, Zr powders combined with sintered solid solution TaB₂–NbC during spark-plasma sintering of compositions at a pressing loading of 60 MPa in the range 1200–1600°C on the phase composition; percent content of Ti, Ta, and Zr in the sialon; microstructure; grain size of crystalline phases; relative density, linear shrinkage, and physical-mechanical properties; and linear correlation of the elasticity modulus and fracture toughness of mullite–β-SiAlON–TiC and mullite–β-SiAlON–*c*-ZrO₂ samples.

EXPERIMENTAL

Mixtures of Al₂O₃ and SiO₂ powders were prepared using Al₂O₃ (Aldrich, Belgium, 97.5% pure) and SiO₂ (Merck, Germany, 97.5% pure). These components were carefully weighed in the weight proportion (3:2) corresponding to stoichiometric mullite (Table 1) and mixed in a planetary ball mill (Retsch, PM 400) for ~10 min.

Powders of β-SiAlON, TiC, TaB₂, and NbC were synthesized at 1660°C in a plasma-chemical unit under vacuum for 1 h through the reactions:

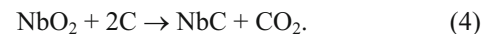
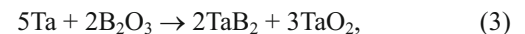
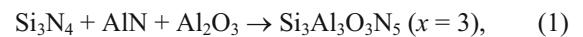


TABLE 1. Characteristics of Starting Components

Obtained powder	Starting components	Manufacturer	Purity, %
β-SiAlON	Si ₃ N ₄ / AlN / Al ₂ O ₃	Merck, Germany / Aldrich, Belgium / Aldrich, Belgium	97.5 / 99.5 / 98.5
TiC	TiO ₂ / C	Merck, Germany / Aldrich, Belgium	98.5 / 98.0
TaB ₂	Ta / B ₂ O ₃	Aldrich, Belgium / Aldrich, Belgium	99.0 / 98.5
NbC	NbO ₂ / C	Merck, Germany / Aldrich, Belgium	98.5 / 98.0
<i>c</i> -ZrO ₂	ZrO ₂ / Y ₂ O ₃	Merck, Germany / Aldrich, Belgium	98.5 / 99.5
Ni	Ni	Merck, Germany	99.5
Ta	Ta	Aldrich, Belgium	99.5
Zr	Zr	Aldrich, Belgium	99.0

Sintered $c\text{-ZrO}_2$ was spark-plasma synthesized at 1400°C under vacuum at a pressing loading of 35 MPa for 2 min using starting components (Table 1) in the ratio corresponding to the phase diagram of the biphasic system $\text{ZrO}_2\text{-Y}_2\text{O}_3$ (Brown and Odell, Fan Fu-K'ang and Keler) [13]. The masses of the components (97 mol% ZrO_2 /3 mol% Y_2O_3) was 94.62/5.38 g per 100 g of mixture; ratio $\text{ZrO}_2/\text{Y}_2\text{O}_3$, 17.58/1.

Sintered solid solution $\text{TaB}_2\text{-NbC}$ was prepared at 1800°C by spark-plasma sintering in vacuum at a pressing loading of 60 MPa for 5 min using TaB_2 and NbC. The masses of the components (mol% TaB_2 /mol% NbC) was 65.64/34.36 g per 100 g of mixture; ratio TaB_2/NbC , 1.91/1.

Sintered $c\text{-ZrO}_2$ and solid solution $\text{TaB}_2\text{-NbC}$ were ground in a planetary ball mill (Retsch PM 400) for 30 min to produce powders of particle sizes from 5 to 10 μm .

Powders of $\beta\text{-SiAlON}$, TiC or sintered $c\text{-ZrO}_2$ powder, and solid solution $\text{TaB}_2\text{-NbC}$ with a mixture of Ni, Ta or Ni, Zr additive were mixed in a planetary ball mill (Retsch PM 400) for ~10 min (Table 2).

The obtained mixture of Al_2O_3 and SiO_2 powders was mixed with the prepared groups of powder mixtures ($\beta\text{-SiAlON/TiC/Ni/Ta/TaB}_2\text{-NbC}$, $\beta\text{-SiAlON/TiC/Ni/Zr/$

$\text{TaB}_2\text{-NbC}$, $\beta\text{-SiAlON}/c\text{-ZrO}_2/\text{Ni/Ta/TaB}_2\text{-NbC}$, and $\beta\text{-SiAlON}/c\text{-ZrO}_2/\text{Ni/Zr/TaB}_2\text{-NbC}$) in a planetary ball mill (Retsch PM 400) for ~10 min for further sintering.

The obtained mixtures of components were loaded into a graphite press die of diameter 30 mm and spark-plasma sintered (SPS, Sumimoto, Model SPS 825. CE, Dr. Sinter, Japan) at 1200 – 1600°C and heating rate 100°C/min under vacuum (6 Pa) at a pressing loading of 60 MPa for 2 min.

Phase compositions of synthesized powders and sintered samples, microstructure, relative density ρ_{rel} , linear shrinkage Δl , elasticity modulus E , Vickers hardness HV , and fracture toughness K_{1c} were determined by well-known methods [7]. The theoretical density (g/cm^3) of the components were mullite 3.17, $\beta\text{-Si}_3\text{Al}_3\text{O}_3\text{N}_5$ 3.09, TiC 4.93, $c\text{-ZrO}_2$ 6.27, TaB_2 11.70, NbC 7.82, Ni_3Ti 7.9, Ni_3Ta 12.0, Ni_3Zr 8.3, NiTi 6.6, NiTa 9.56, NiZr 7.4, and NiZr_2 7.2.

RESULTS AND DISCUSSION

The phase compositions of the synthesized sialon and TiC powders showed strong diffraction maxima for $\beta\text{-SiAlON}$ and TiC with small amounts of unreacted AlN and titanium oxycarbide, respectively (Fig. 1). The crystalline

TABLE 2. Weight Proportions and Ratio of Components in Starting Powder Mixtures*

Parameters	Composition			
	M20SiAl3TiC25Ni 25Ta27(50TaB ₂ - 50NbC)	M20SiAl3TiC25Ni 25Zr27(50TaB ₂ - 50NbC)	M20SiAl3ZrO ₂ 25Ni 25Ta27(50TaB ₂ - 50NbC)	M20SiAl3ZrO ₂ 25Ni 25Zr27(50TaB ₂ - 50NbC)
Mass of components, g per 100 g of mixture:				
20 mol% $\beta\text{-Si}_3\text{Al}_3\text{O}_3\text{N}_5$ / 3 mol% TiC / 25 mol% Ni / 25 mol% Ta / 27 mol% (50TaB ₂ -50NbC)	35.21 / 1.12 / 9.01 / 28.15 / 26.51	—	—	—
20 mol% $\beta\text{-Si}_3\text{Al}_3\text{O}_3\text{N}_5$ / 3 mol% TiC / 25 mol% Ni / 25 mol% Zr / 27 mol% (50TaB ₂ -50NbC)	—	41.18 / 1.31 / 10.54 / 16.54 / 30.43	—	—
20 mol% $\beta\text{-Si}_3\text{Al}_3\text{O}_3\text{N}_5$ / 3 mol% $c\text{-ZrO}_2$ / 25 mol% Ni / 25 mol% Ta / 27 mol% (50TaB ₂ -50NbC)	—	—	35.0 / 2.28 / 8.96 / 28.0 / 25.76	—
20 mol% $\beta\text{-Si}_3\text{Al}_3\text{O}_3\text{N}_5$ / 3 mol% ZrO_2 / 25 mol% Ni / 25 mol% Zr / 27 mol% (50TaB ₂ -50NbC)	—	—	—	40.65 / 2.65 / 10.41 / 16.32 / 29.97
Ratio of $3\text{Al}_2\text{O}_3\cdot 2\text{SiO}_2$ / $\beta\text{-Si}_3\text{Al}_3\text{O}_3\text{N}_5$ / TiC / Ni / Ta / 50TaB ₂ -50NbC, $3\text{Al}_2\text{O}_3\cdot 2\text{SiO}_2$ / $\beta\text{-Si}_3\text{Al}_3\text{O}_3\text{N}_5$ / TiC / Ni / Zr / 50TaB ₂ -50NbC, $3\text{Al}_2\text{O}_3\cdot 2\text{SiO}_2$ / $\beta\text{-Si}_3\text{Al}_3\text{O}_3\text{N}_5$ / $c\text{-ZrO}_2$ / Ni / Ta / 50TaB ₂ -50NbC, $3\text{Al}_2\text{O}_3\cdot 2\text{SiO}_2$ / $\beta\text{-Si}_3\text{Al}_3\text{O}_3\text{N}_5$ / $c\text{-ZrO}_2$ / Ni / Zr / 50TaB ₂ -50NbC	2.84 / 89.28 / 11.1 / 3.55 / 3.77	2.42 / 76.33 / 9.48 / 6.04 / 3.28	2.85 / 43.86 / 11.16 / 3.57 / 3.88	2.46 / 37.73 / 9.60 / 6.12 / 3.34

* Mass of components ($3\text{Al}_2\text{O}_3/2\text{SiO}_2$) is 71.8/28.2 g per 100 g of mixture.

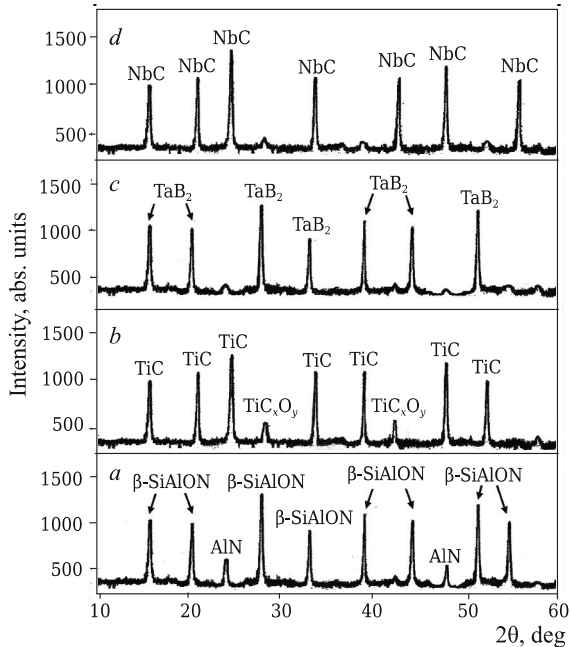


Fig. 1. Phase composition of powders of β -SiAlON (a), TiC (b), TaB₂ (c), and NbC (d) synthesized by plasma-chemical method at 1600°C: TiC_xO_y is titanium oxycarbide.

phase TiC_xO_y was nonstoichiometric TiC. It contained unreacted TiO₂ and C. The obtained TaB₂ and NbC powders consisted of developed TaB₂ and NbC crystalline phases.

Sintered *c*-ZrO₂ was characterized by distinct diffraction maxima of this phase (Fig. 2). This was explained by incorporation (intercalation) of Y³⁺ cations into the crystal structure of tetragonal ZrO₂ that stimulated rearrangement of tetragonal into cubic ZrO₂ with formation of the solid solution of (cubic) ZrO₂ at 1400°C at a pressing load of 35 MPa according to the equilibrium phase diagram of the ZrO₂–Y₂O₃ system (Brown and Odell, Fan Fu-K'ang and Keler) [13].

The x-ray pattern of sintered solid solution TaB₂–NbC showed stronger diffraction maxima of (Nb,Ta)C,B and weaker, of (Ta,Nb)B,C (Fig. 3). This was explained by more active incorporation (intercalation) of small-sized Ta⁴⁺ into the dense (cubic) NbC structure as compared to the less vigorous incorporation of large-sized Nb⁴⁺ into the less dense (hexagonal) TaB₂ structure. The difference in the intensities of the (Nb,Ta)C,B and (Ta,Nb)B,C diffraction maxima was explained by the large difference in the sizes of the Ta⁴⁺ and Nb⁴⁺ cations and, as a result, the different extents of the structure-formation processes of the solid solutions in the solids at a pressing loading of 70 MPa. The size effect of Ta⁴⁺ and Nb⁴⁺ was proportional to the development of the (Nb,Ta)C,B and (Ta,Nb)B,C crystalline phases and corresponded to the ratio of TaB₂ and NbC. The microstructure of sintered solid solution TaB₂–NbC was crystalline, partially nonuniformly sintered, and variously agglomerated with a small amount of variously sized pores, in particular, in the crystalline (Nb,Ta)C,B region in which densely sintered

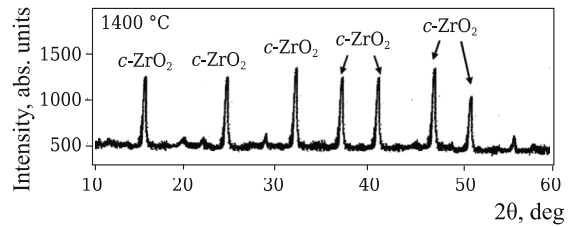


Fig. 2. Phase composition of *c*-ZrO₂ spark-plasma synthesized at 1400°C.

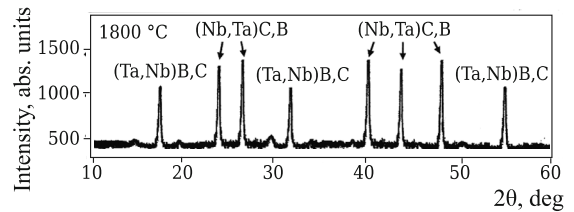


Fig. 3. Phase composition of binary solid solution TaB₂–NbC (ratio 50TaB₂–50NbC) spark-plasma sintered at 1800°C: (Nb,Ta)C,B — solid solution of tantalum borocarbide; (Ta,Nb)B,C — solid solution of niobium carboboride.

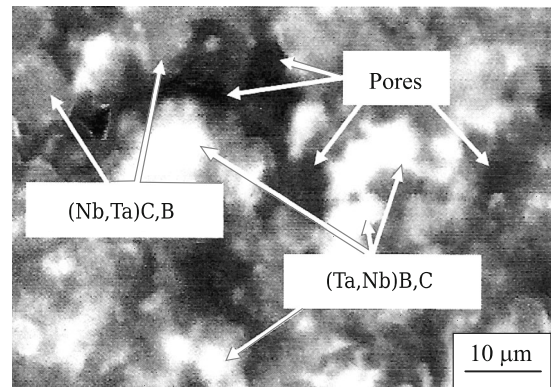


Fig. 4. Microstructure of solid solution TaB₂–NbC (ratio 50TaB₂–50NbC) spark-plasma sintered at 1800°C with indication of crystalline regions (Nb,Ta)C,B and (Ta,Nb)B,C.

(Ta,Nb)B,C particles were noticeable (Fig. 4). This microstructure was due to active incorporation of the small Ta⁴⁺ cation into the dense (cubic) NbC structure, as a result of which TaB₂ stimulated sintering to a lesser extent and was mainly consumed for crystallization of (Nb,Ta)C,B (Fig. 3). This slowed solid-state sintering of (Nb,Ta)C,B and (Ta,Nb)B,C grains. Densely sintered particles of (Ta,Nb)B,C with a crystalline (Nb,Ta)C,B region formed because of the less developed crystallization of (Ta,Nb)B,C (Fig. 4), during the course of which mainly NbC stimulated sintering in combination with dense compaction of sintered TaB₂ and NbC particles. As a result, TaB₂ and NbC particles were more uniformly and strongly sintered. Boundary grains of these solid solutions were densified and strengthened as compared to

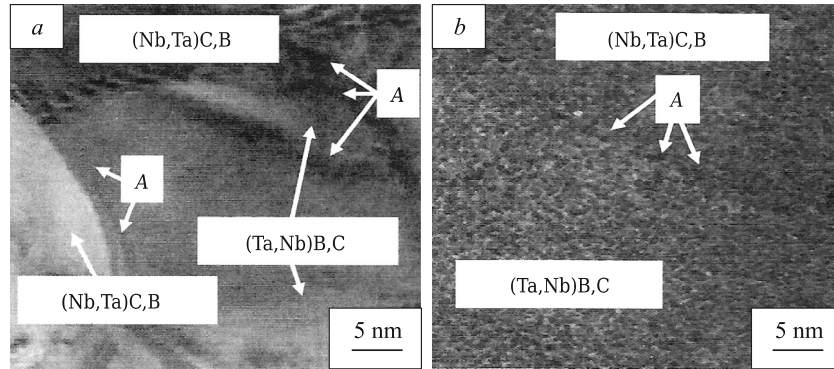
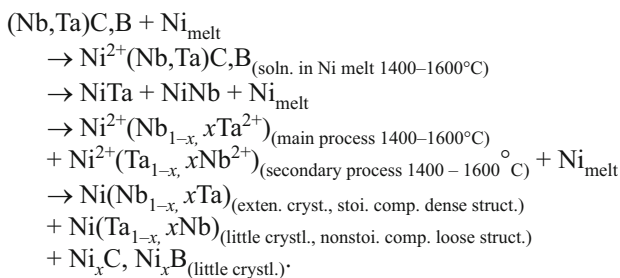


Fig. 5. Microstructure of solid solution 50TaB₂-50NbC sintered at 1800°C with designation of grain boundaries (a) and regions (b) of (Nb,Ta)C,B and (Ta,Nb)B,C: A is boundary layer of (Nb,Ta)C,B.

formation of an intermediate layer of (Nb,Ta)C,B in the boundary parts of sintered TaB₂ and NbC particles. The brittleness and extent of developed elastic properties at the boundaries of (Nb,Ta)C,B and (Ta,Nb)B,C particles were significantly reduced (Fig. 5).

Figure 6 shows the phase composition of samples spark-plasma sintered in the range 1200 – 1600°C.

Samples with Ni, Ta and Ni, Zr mixtures were characterized by extensive mullitization and greater crystallization of (Nb,Ta)C,B than the less developed crystalline (Ta,Nb)B,C in the range 1400 – 1600°C. Mullite appeared because of active dissolution of Al₂O₃ and SiO₂ in the nickel melt with the formation and structuring of stoichiometric mullite via this melt. Copious crystallization of (Nb,Ta)C,B was explained by the poorer dissolution of the less dense (Nb,Ta)C,B in the nickel melt in the range 1400 – 1600°C. Extensive crystalline Ni(Nb,Ta) was observed in the samples, the development of which was similar in amount to crystalline (Nb,Ta)C,B. Also, the lack of crystalline Ni(Ta,Nb) was notable in the range 1400 – 1600°C (Fig. 6a–d). This was related to the low solubility of (Ta,Nb)B,C in the nickel melt. Crystalline Ni(Nb,Ta) had a different composition than (Nb,Ta)C,B in the range 1400 – 1600°C (Fig. 6a–d). In particular, it contained only metallic components. Hence, crystalline Ni(Nb,Ta) was a metallic phase. The phase Ni(Nb,Ta) was initiated at 1400°C in the nickel melt and developed in the nickel melt saturated (eutectic) in the range 1400 – 1500°C and supersaturated (peritectic) in the range 1500 – 1600°C at a pressing loading of 60 MPa via the reactions:



Different amounts of crystalline β -SiAlON were noticeable in the samples. It was more abundant in samples with TiC, Ta and TiC, Zr mixtures than in samples with *c*-ZrO₂, Ta and *c*-ZrO₂, Zr mixtures in the range 1200 – 1600°C (Fig. 6). This was due to more active incorporation of smaller Ti⁴⁺ and Ta⁴⁺ cations and larger Zr⁴⁺ cations into the tetrahedral AlN_xO_{4-x} structure and partially into the tetrahedral SiN_xO_{4-x} structure of sialon with better dissolution of TiC, Ta and TiC, Zr mixtures in the nickel melt as compared to gradual dissolution of *c*-ZrO₂, Ta and *c*-ZrO₂, Zr in it.

The samples showed weak peaks for crystalline Ni₃Ti, Ni₃Ta, and Ni₃Zr in the range 1200 – 1300°C (Fig. 6a–d). Crystalline Ni₃Ti formed through congruent melting of Ni₃Ti₃ + NiTi \leftrightarrow Ni₃Ti at 1140°C; crystalline Ni₃Ta, through peritectic reaction Ni₈Ta \leftrightarrow Ni₈ + Ni₃Ta at 1150°C and eutectic reaction Ni₈Ta_{melt} \leftrightarrow Ni₈ + Ni₃Ta at 1230°C; crystalline Ni₃Zr, through peritectic reactions Ni₇Zr₂ + Ni₂₁Zr₈ \leftrightarrow Ni₃Zr and Ni₇Zr₂ + Ni₅Zr₂ \leftrightarrow Ni₃Zr at 1170°C in the equilibrium diagrams of biphasic Ni–Ti, Ni–Ta, and Ni–Zr [14 – 16]. As a result, development of crystalline TiC and *c*-ZrO₂ in the range 1200 – 1300°C was somewhat slowed (Fig. 6a–d).

A slight ingrowth of crystalline NiTi was observed in the samples in the range 1500 – 1600°C (Fig. 6a and b). It formed through the peritectic reaction melt + Ni₃Ti \leftrightarrow NiTi at 1400°C. This agreed with the equilibrium diagram of the biphasic Ni–Ti system [14]. Poor development of crystalline NiTi was due to more active incorporation of Ti⁴⁺ into the tetrahedral AlN_xO_{4-x} structure of sialon (Fig. 6a and b).

A large amount of crystalline NiTa was observed in the samples in the range 1500 – 1600°C (Fig. 6a and c). It formed through the eutectic reaction melt \leftrightarrow Ni₂Ta + NiTa at 1350°C with initiation of NiTa crystallization at 1400°C. The occurrence of this reaction assisted dissolution of Ni₃Ta in the melt and formation of Ni₂Ta through the peritectic reaction melt + Ni₃Ta \leftrightarrow Ni₂Ta at 1400°C. These processes agreed with the equilibrium diagram of the biphasic Ni–Ta system [15, 17].

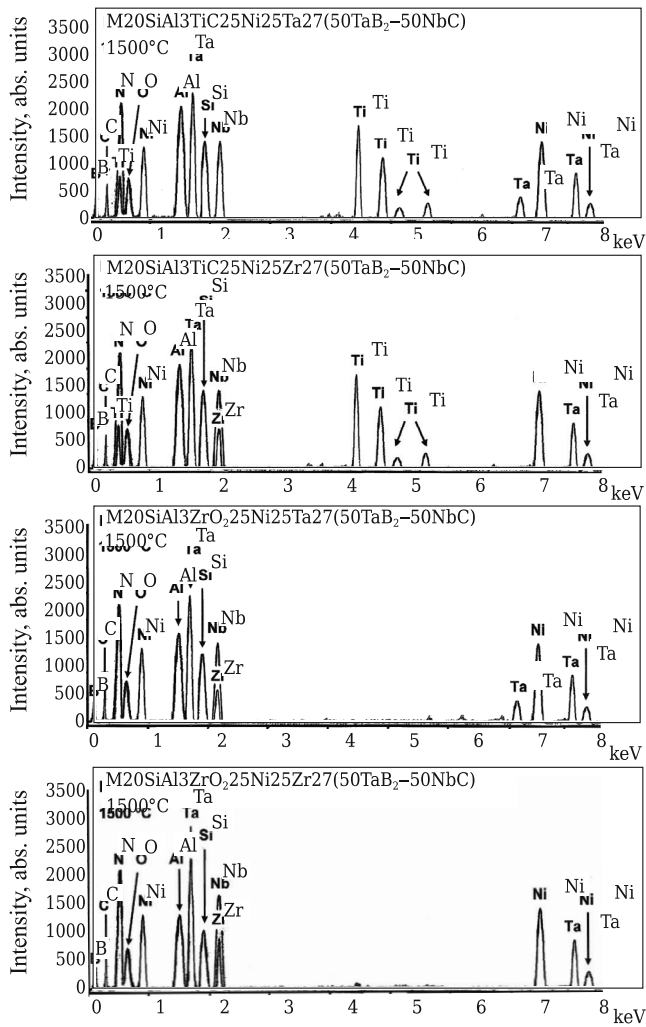


Fig. 7. Elemental composition and peak intensities of crystalline phases in samples sintered at 1500°C.

with the equilibrium diagram of the biphasic Ni–Zr system [16, 18].

Reactions of mullite, β -SiAlON, and c -ZrO₂ with TiC, solid solutions, and intermetallic compounds of various com-

positions were not observed because decomposition products of mullite and sialon and oxidation of sialon; TiC; (Nb,Ta)C,B; Ni(Nb,Ta); (Ta,Nb)B,C; NiTi; NiTa; NiZr; and NiZr₂ were missing in the range 1200 – 1600°C. Also, reactions between TiC; c -ZrO₂; (Nb,Ta)C,B; and (Ta,Nb)B,C with Ta and Zr powders were not observed. This was due to the better dissolution of Ta and Zr powders in the nickel melt. As a result, additional diffraction maxima and their shifting in the range 1200 – 1600°C were not observed.

Figure 7 shows the composition, peak intensities of elements of crystalline phases, and the effects of Ti⁴⁺, Ta⁴⁺, and Zr⁴⁺ on the growth of sialon Si and Al peaks of samples sintered at 1500°C as studied by energy dispersive x-ray spectroscopy.

The intensities of the element peaks of the crystalline phases (Fig. 7) agreed with the development of the crystalline phases of the sample at 1500°C (Fig. 6a – d). The Si and Al peaks had different intensities in the samples sintered at 1500°C because the mullite and sialon crystalline phases were actively structured by the nickel melt (Fig. 6a – d). The positions of the Si and Al peaks in mullite and sialon coincided because the Si and Al cations in both compounds were identically coordinated and located in similar polyhedral positions of the crystal structures of these phases. On the other hand, the more active incorporation of Ti⁴⁺, Ta⁴⁺ and Ti⁴⁺, Zr⁴⁺ into the tetrahedral AlN_xO_{4-x} sialon structure because of extensive dissolution of TiC, Ta and TiC, Zr mixtures in the nickel melt facilitated formation of strong Si and Al peaks, in contrast to the weaker Si and Al peaks for less active incorporation of Zr⁴⁺, Ta⁴⁺ and Zr⁴⁺, Zr⁴⁺ into the tetrahedral AlN_xO_{4-x} sialon structure because of gradual dissolution of c ZrO₂, Ta and c ZrO₂, Zr mixtures in the nickel melt. The strong Ti peak (4.5 keV) was due to active incorporation of Ti⁴⁺ into the tetrahedral AlN_xO_{4-x} sialon structure. As a result, the percent content of Si and Al, Ti/Ta, and Ti/Zr was noticeably greater in sialon of samples with TiC, Ta and TiC, Zr mixtures, in contrast with the percent content of Si and Al, Zr/Ta, and Zr/Zr in sialon of samples with c -ZrO₂, Ta and c -ZrO₂/Zr mixtures (Table 3). The strong Ta peak (1.70 keV) and weaker Nb peak (2.2 keV) were due to extensive crystallization of (Nb,Ta)C,B and Ni(Nb,Ta) and less crystalline

TABLE 3. Percent Content of Si and Al, Ti, Ta, Zr in Sialon*

Composition	Content, %						
	Si	Al	O	N	Ti / Ta	Ti / Zr	Zr / Ta
M20SiAl3TiC25Ni25Ta27(50TaB ₂ -50NbC)	19.35	42.60	12.22	11.70	6.40/7.73	—	—
M20SiAl3TiC25Ni25Zr27(50TaB ₂ -50NbC)	18.82	40.68	11.82	11.64	—	10.47/6.57	—
M20SiAl3ZrO ₂ 25Ni25Ta27(50TaB ₂ -50NbC)	17.94	38.97	11.60	11.25	—	—	11.95/8.29
M20SiAl3ZrO ₂ 25Ni25Zr27(50TaB ₂ -50NbC)	16.82	36.73	11.46	11.12	—	—	11.64/12.23

* Percent content of Si, Al, O, N and Ti, Ta, Zr in sialon determined from diffraction maxima intensities of sialon and (Nb,Ta)C,B; Ni(Nb,Ta); (Ta,Nb)B,C; NiTi; NiTa; NiZr; NiZr₂ at 1500°C (Fig. 6a – d); uncertainty of content of which was ±0.3, ±0.35, ±0.2, ±0.31 and ±0.31, ±0.35, ±0.38, respectively. Total content of Si, Al, O, N and Ti, Ta, Zr in sialon samples at 1500°C equaled 100%.

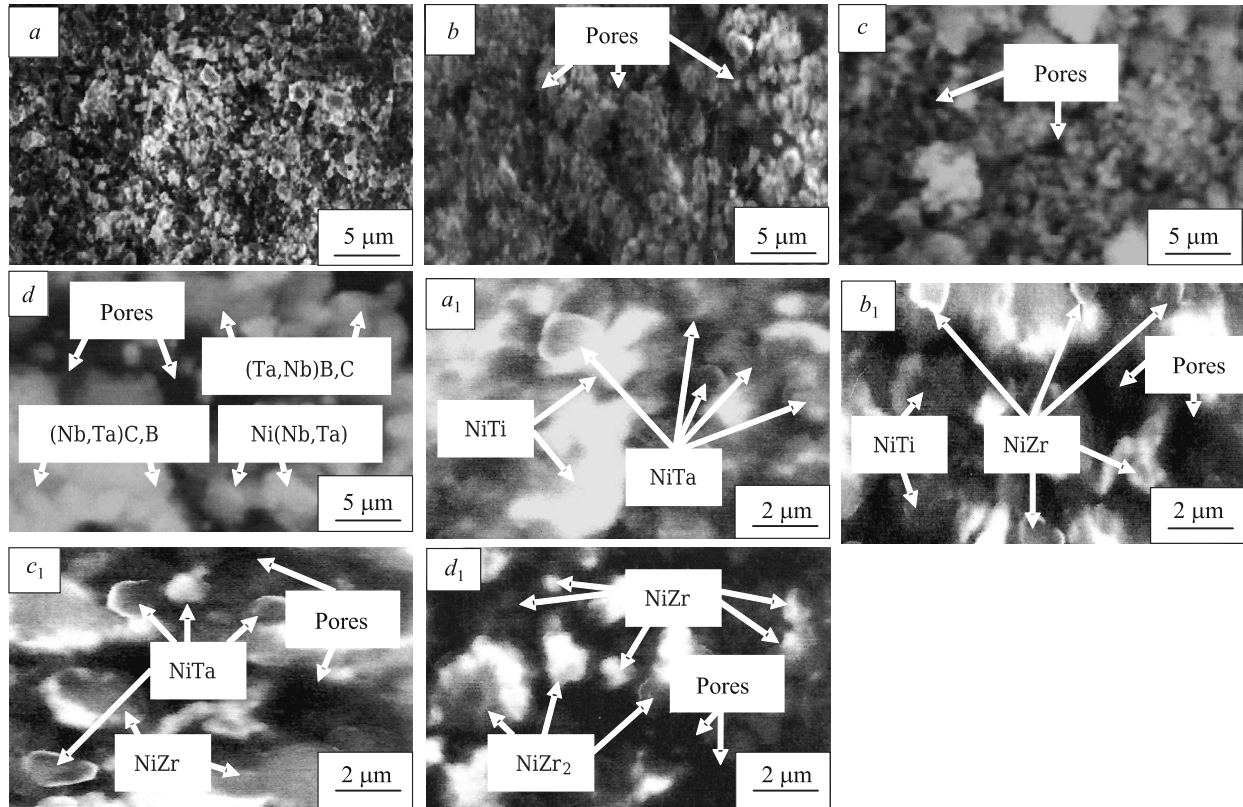


Fig. 8. Microstructure of ceramic ($a-d$) and metallic phases (a_1-d_1) of M20SiAl3TiC25Ni25Ta27(50TaB₂-50NbC) (a, a_1), M20SiAl3TiC25Ni25Zr27(50TaB₂-50NbC) (b, b_1), M20SiAl3ZrO₂25Ni25Ta27(50TaB₂-50NbC) (c, c_1), and M20SiAl3ZrO₂25Ni25Zr27(50TaB₂-50NbC) (d, d_1) sintered at 1500°C.

(Ta,Nb)B,C at 1500°C, respectively (fig. 6a-d). The strong Ni peaks (0.85 and 7.5 keV) in combination with medium peaks for Ti (0.5 and 4.9 keV), Ta (8.18 keV), and Zr (2.2 keV) were due to formation of crystalline NiTi, NiTa, and NiZr, respectively, at 1500°C (Fig. 6a-c). A stronger and narrower Zr peak (2.2 keV) was noticeable in the sample with the *c*-ZrO₂, Zr mixture. This was explained by dissolution of NiZr in the eutectic melts formed from Ni₇Zr₂ + Ni₁₁Zr₉ and Ni₁₀Zr₇ + Ni₂₁Zr₈ with formation of a peritectic melt of composition Ni₁₁Zr₉, through which NiZr₂ crystallized at 1500°C (Fig. 6d). Simultaneously, the Nb peak (2.2 keV) was stronger than the Zr peak (2.2 keV) in the samples. This was due to greater crystallization of (Ta,Nb)B,C as compared to lesser crystallization of NiZr and NiZr₂ at 1500°C (Fig. 6b-d). Also, the observed weak Ti (5.17 and 5.52 keV) and Ta (7.18 keV) peaks were related to little and incomplete crystallization of NiTi and NiTa phases, respectively, at 1500°C (Fig. 6a-c) because of extensive incorporation of Ti⁴⁺ and Ta⁴⁺ into the tetrahedral AlN_xO_{4-x} sialon structure during dissolution of TiC and Ta in the nickel melt at 1500°C (Fig. 6a-c).

The different effects of Ti⁴⁺, Ta⁴⁺, and Zr⁴⁺ on the evolution of the sialon Si and Al peaks had different effects on the percent content of Si and Al, Ti, Ta, and Zr in the sialon samples at 1500°C (Table 3).

The microstructure of the ceramic phase of the sample with the TiC, Ta mixture was more uniformly and densely sintered, finely grained, and pore-free (Fig. 8a) because of the equally vigorous and complete incorporation of Ti⁴⁺ and Ta⁴⁺ into the tetrahedral AlN_xO_{4-x} sialon structure (Fig. 6a). This was consistent with rapid diffusion through the sialon oxide component and uniform sintering of sialon particles with (Ta,Nb)B,C; (Nb,Ta)C,B; and Ni(Nb,Ta) particles. The microstructure of the ceramic phase in the sample with the *c*-ZrO₂, Ta mixture was about the same (Fig. 8c) and contained separately positioned agglomerates of various sizes and a slightly greater number of small pores. The smaller agglomerates consisted of weakly sintered particles of sialon and (Ta,Nb)B,C; large agglomerates, of highly sintered sialon; (Nb,Ta)C,B; and Ni(Nb,Ta) particles. These agglomerates formed because of the more nonuniform sintering of these particles resulting from slower diffusion through the sialon oxide component during nonuniform incorporation of Zr⁴⁺ and Ta⁴⁺ into the tetrahedral AlN_xO_{4-x} sialon structure (Fig. 6c). Such sintering led to incomplete pore filling.

Samples with the TiC, Zr and *c*-ZrO₂, Zr mixtures had a noticeably more uniformly sintered ceramic-phase microstructure with a significant content of agglomerates of various sizes consisting of variously sintered particles of (Nb,Ta)C,B; Ni(Nb,Ta); and (Ta,Nb)B,C and large pores

(Fig. 8*b* and *d*). Denser monolithic agglomerates of (Nb,Ta)C,B and Ni(Nb,Ta) of sizes up to 5 – 8 μm formed, in contrast to the less dense agglomerates of (Ta,Nb)B,C of sizes 2.5 – 5 μm . This was related to the different extents of recrystallization of (Nb,Ta)C,B, Ni(Nb,Ta), and (Ta,Nb)B,C particles and dissolution of Zr powder with TiC and *c*-ZrO₂ in the Ni melt, during which a eutectic melt of NiZr and a peritectic melt of NiZr₂ of different viscosities formed in the sintered compositions with TiC, Zr and *c*-ZrO₂, Zr. This affected the uniformity and rate of diffusion through the nickel melt and; therefore, the rate of recrystallization of the particles and the homogeneity of the shapes and sizes of the agglomerates of the solid solutions of the ceramic and metallic phases. As a result, the microstructure of the ceramic phase of the sample with *c*-ZrO₂, Zr was less uniform and highly agglomerated (Fig. 8*d*).

The microstructure of the metallic phases (Fig. 8, *a*₁ and *c*₁) corresponded to the microstructure of the ceramic phases of the samples with the TiC, Ta and *c*-ZrO₂, Ta mixtures (Fig. 8*a* and *c*). However, several differences were seen in the microstructure of the metallic phases, in particular, the NiTi particles were more densely sintered as soft agglomerates of sizes 2 – 5 μm upon dissolution of TiC, *c*-ZrO₂ in the nickel melt (Fig. 8*a*₁), in contrast to the separately positioned and large NiZr particles of sizes 2 – 2.5 μm , between which pores were observed (Fig. 8*c*₁).

Partially sintered NiTa particles formed during dissolution of Ta powder in the nickel melt as soft agglomerates consisting of smaller NiTa particles (Fig. 8*a*₁) than separately positioned small rounder NiTa particles (Fig. 8*c*₁). The structures and shapes of the NiTi, NiZr, and NiTa particles differed because of the different formation reactions of crystalline NiTi, NiZr, and NiTa phases in the corresponding NiTi peritectic melt and NiZr and NiTa eutectic melts at 1500°C.

In turn, the microstructures of the metallic phases (Fig. 8*b*₁ and *d*₁) were more uniform and contained many pores when compared to the microstructures of the ceramic phases of the samples with TiC, Zr and *c*-ZrO₂, Zr mixtures (Fig. 8*b* and *d*). Weakly sintered NiTi particles as soft agglomerates of sizes ~2.5 μm (Fig. 8*b*₁) were noticeable in the microstructure of the metallic phases upon dissolution of TiC and *c*-ZrO₂ in the nickel melt, in contrast to more rounded smaller NiZr particles of sizes 0.5 – 1 μm (Fig. 8*d*₁). The NiTi and NiZr particles were separated from each other by pores. The differences in the structures and shapes of the NiTi and NiZr particles were related to the different formation reactions of the crystalline NiTi and NiZr/NiZr₂ phases in the peritectic NiTi melt and the eutectic/peritectic NiZr/NiZr₂ melts at 1500°C. As a result, the compounds diffused unevenly between the sintered NiTi and NiZr particles with nonuniform and incompletely filled pores (Fig. 8*b*₁ and *d*₁).

The NiZr particles that formed in the presence of NiTi during dissolution of Zr powder in the nickel melt were more rounded and smaller (to 1 μm) (Fig. 8*b*₁) than the NiZr parti-

cles that were more agglomerated and larger (1 – 1.5 μm) in the presence of NiZr (Fig. 8*d*₁). This was explained by the different formation reactions of the crystalline NiTi and NiZr/NiZr₂ phases in the NiTi peritectic melt and the NiZr/NiZr₂ eutectic/peritectic melt at 1500°C. Separately positioned dense NiZr₂ agglomerates of various sizes were observed in the sample with the *c*-ZrO₂, Zr mixture (Fig. 8*d*₁). This was related to dissolution of particles of crystalline NiZr phase in eutectic melts at 1300°C with formation of the Ni₁₁Zr₉ peritectic melt at 1500°C, in which nonuniform recrystallization (growth) of NiZr₂ particles occurred, slowed most the sintering of NiZr and NiZr₂ particles, and caused irregular and incomplete pore filling.

Figures 9 – 13 show the grain sizes of the crystalline phases, ρ_{rel} and Δl in the range 1200 – 1600°C, the microstructure of the boundary regions of oxide and oxide-free crystalline phases at 1500°C, the physical-mechanical properties in the range 1200 – 1600°C, and photographs of indentations at 1500°C of samples with TiC, Ta; *c*-ZrO₂, Ta; TiC, Zr; and *c*-ZrO₂, Zr mixtures.

The quantities ρ_{rel} and Δl of samples with TiC, Ta and *c*-ZrO₂, Ta mixtures changed dramatically and uniformly in the range 1200 – 1600°C because β -SiAlON rapidly crystallized, approximately equal to crystallization of the (Nb,Ta)C,B and Ni(Nb,Ta) phases (Fig. 6*a* and *c*); particles of sialon, TiC, and *c*-ZrO₂ sintered uniformly with particles of (Nb,Ta)C,B, Ni(Nb,Ta), and (Ta,Nb)B,C; evenly and densely sintered microstructures of ceramic phases formed in the nickel melt (Fig. 8*a* and *c*); and a polydisperse composition of crystalline phase grains developed (Fig. 9). The composition with the TiC, Ta mixture sintered somewhat more extensively with large increases of ρ_{rel} and Δl than the composition with the *c*-ZrO₂, Ta mixture. This correlated with several differences in the microstructures of the ceramic and metallic phases (Fig. 8*a*, *c*, *a*₁, *c*₁) and the grain size distribution of the crystalline phases (Fig. 9). These differences were explained by faster diffusion processes in the peritectic NiTi melt and eutectic NiTa melt, in contrast to slower diffusion in the eutectic NiZr and NiTa melts. As a result, pores in the ceramic and metallic phases of sintered compositions filled differently (Fig. 8*a*, *c*, *a*₁, *c*₁). The ρ_{rel} and Δl values of the sample with the *c*-ZrO₂, Ta mixture were close to those of the sample with the TiC, Ta mixture in the range 1500 – 1600°C. This was due to the formation of NiZr and NiTa particles of a different shape (Fig. 8*c*₁) and a more polydisperse grain composition of the crystalline phases (Fig. 9) than of the NiTi and NiTa particles as soft agglomerates (Fig. 8*a*₁).

The ρ_{rel} and Δl values of the sample with the TiC, Zr mixture increased in the range 1200 – 1600°C because diffusion processes in the solid phase during congruent melting with Ni₃Ti₃ and peritectic reactions with Ni₇Zr₂, Ni₂₁Zr₈ and Ni₅Zr₂, Ni₅Zr₂ were unequal and incomplete in the range 1200 – 1300°C, a nonuniformly sintered microstructure of the ceramic phase with agglomerates and many variously sized pores formed (Fig. 8*b*), diffusion processes in the me-

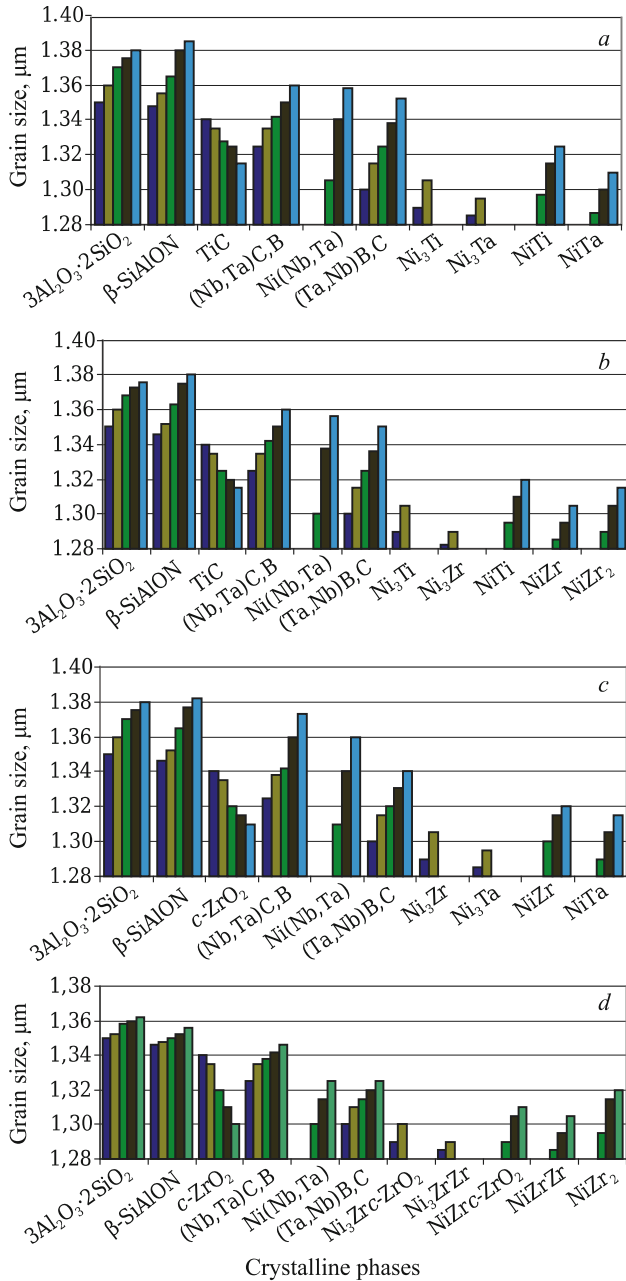


Fig. 9. Grain sizes of crystalline phases of M20SiAl3TiC25Ni25Ta27(50TaB₂–50NbC) (a), M20SiAl3TiC25Ni25Zr27(50TaB₂–50NbC) (b), M20SiAl3ZrO₂25Ni25Ta27(50TaB₂–50NbC) (c), and M20SiAl3ZrO₂25Ni25Zr27(50TaB₂–50NbC) (d) sintered in the range 1200 – 1600°C: ■) 1200°C; ■) 1300°C; ■) 1400°C; ■) 1500°C; ■) 1600°C.

tallic phase were slower and variously sintered NiTi and NiZr particles of various shapes and sizes formed (Fig. 8b₁), and a relatively monodisperse grain composition of the crystalline phases developed (Fig. 9).

The quantities ρ_{rel} and Δl of the sample with the *c*-ZrO₂, Zr mixture evolved nonuniformly. In particular, the values of these properties increased smoothly up to 1400°C and de-

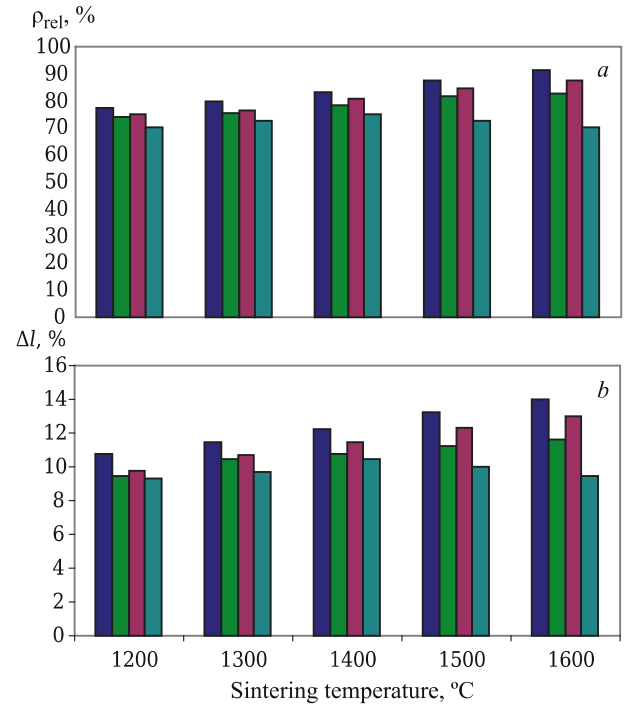


Fig. 10. Evolution of ρ_{rel} (a) and Δl (b) of M20SiAl3TiC25Ni25Ta27(50TaB₂–50NbC) (■), M20SiAl3TiC25Ni25Zr27(50TaB₂–50NbC) (■), M20SiAl3ZrO₂25Ni25Ta27(50TaB₂–50NbC) (■), and M20SiAl3ZrO₂25Ni25Zr27(50TaB₂–50NbC) (■) sintered in the range 1200 – 1600°C.

creased in the range 1400 – 1600°C. The properties increased smoothly up to 1400°C because of unequal and incomplete diffusion in the solid phase during peritectic reactions with Ni₇Zr₂, Ni₂₁Zr₈ and Ni₇Zr₂, Ni₅Zr₂ in the range 1200 – 1300°C. The ρ_{rel} and Δl values decreased in the range 1400 – 1600°C because of the formation of a more nonuniformly sintered ceramic phase microstructure with recrystallization of (Nb,Ta)C,B, Ni(Nb,Ta), and (Ta,Nb)B,C particles (Fig. 8d); slower diffusion in the metallic phase with partial recrystallization of NiZr particles; rapid recrystallization of NiZr₂ particles (Fig. 8d₁); and formation of a more monodisperse grain composition of the crystalline phases (Fig. 9).

The evolution of the physical-mechanical properties of samples with added Ta, Zr corresponded to sintering of these compositions in the range 1200 – 1600°C. The quantities E and K_{1c} increased most for samples with TiC, Ta and *c*-ZrO₂, Ta mixtures. The HV values were observed to increase evenly with minor differences in samples with the TiC, Zr mixture. The difference was much more substantial for the E values of these samples than for the K_{1c} values. The sample with the *c*-ZrO₂, Zr mixture showed nonuniform evolution of the properties in the range 1200 – 1600°C.

The more developed E and K_{1c} values of samples with TiC, Ta and *c*-ZrO₂, Ta mixtures were due to the variety of crystalline formations; the different shapes and sizes of NiTi,

NiTa, and NiZr particles (Fig. 8a₁, c₁); the polydisperse grain composition of the crystalline phases (Fig. 9); and the positioning of regions of NiTi, NiTa, and NiZr of different sizes in crystalline structures of the ceramic and metallic phases, in their boundary layers (Fig. 11a₂, a₃, c₂, c₃), and at grain boundaries as thin intermediate layers, separate regions, and grains between them (Fig. 11a₂₋₀, a₃₋₀, c₂₋₀, c₃₋₀). The uniform microstructures (Fig. 8a₁, c₁) and polydisperse grain composition of the crystalline phases (Fig. 9) promoted densification of differently sized particles and increased the structural rigidity. Finely disperse particles with dense NiTi (cubic), NiTa, and NiZr (rhombohedral) structures hardened regions of the ceramic and metallic phases and boundary layers and stimulated more uniform and complete dissipation of stresses in boundary particles of the ceramic and metallic phases and even distribution of plastic properties in the structures of NiTi, NiTa, and NiZr crystalline phases and in boundary layers. As a result, homogeneous and narrow boundary layers of mullite-β-SiAlON-*c*-ZrO₂ and (Ta,Nb)B,C-(Nb,Ta)C,B-Ni(Nb,Ta) were observed (Fig. 11a - a₂, c - c₂) and helped to densify, strengthen, and evolve the plastic properties of these boundary layers. Expanding microcracks interacted extensively with particles of these phases and NiTi and NiTa as soft agglomerates during the most even and complete dissipation of stresses in boundary particles of the ceramic and metallic phases, in contrast to the less vigorous interaction of the microcracks with separately positioned large NiTa and NiZr particles. High crack resistance without microcracks was noticed in the sample with the TiC, Ta mixture (Fig. 13a₁) as compared to slight damage and several shallow chips around the indentation of the sample with the *c*-ZrO₂, Ta mixture (Fig. 13c₁). The crack resistance of these samples was much greater at 1500°C than at 1300°C, where rapid propagation of several microcracks along linear (Fig. 13a) and tortuous paths with large chips around the indentation (Fig. 13c) were observed. This was related to nonuniform and incomplete solid-state diffusion processes because of congruent melting with Ni₃Ti₃ at 1140°C, a peritectic reaction with Ni₈Ta at 1150°C, and a eutectic reaction with Ni₈Ta at 1230°C in the sintered composition with the TiC, Ta mixture (Fig. 6a) and a peritectic reaction with Ni₇Zr₂, Ni₂₁Zr₈ and Ni₇Zr₂, Ni₅Zr₂ at 1170°C, a peritectic reaction with Ni₈Ta at 1150°C, and a eutectic reaction with Ni₈Ta at 1230°C in the sintered composition with the *c*-ZrO₂, Ta mixture (Fig. 6c) caused by their nonuniform sintering in the range 1200 - 1300°C (Fig. 10). In general, these results correlated with the change of K_{1c} and HV in the range 1200 - 1600°C.

The nonuniform and slower evolution of the physical-mechanical properties of the samples with the TiC, Zr and *c*-ZrO₂, Zr mixtures was explained by the nonuniformly sintered microstructure of the ceramic phases that consisted of variously sintered agglomerates of (Ta,Nb)B,C, (Nb,Ta)C,B, and Ni(Nb,Ta) (Fig. 8b and d); weakly sintered NiTi and NiZr particles of various shapes and sizes (Fig. 8b₁); large NiZr grains and variously sized dense NiZr₂ agglomerates (Fig. 8d₁); the different monodisperse compo-

sition of grains of crystalline phases (Fig. 9); the location of NiTi, NiZr, and NiZr₂ regions at different distances from the boundary layers of crystalline ceramic and metallic phases (Fig. 11b₂, b₃, d₂, d₃) with intermediate layers of various widths on the boundary grains and separate regions between them (Fig. 11b₂₋₀, b₃₋₀, d₂₋₀, d₃₋₀). The nonuniformity of the microstructures (Fig. 8b, d, b₁, d₁) and the different monodisperse composition of crystalline phase grains (Fig. 9) caused uneven densification of the particles and reduction of the structural rigidity. Particles with dense NiTi (cubic), NiZr (rhombohedral), and NiZr₂ structures (tetragonal) caused regions of ceramic and metallic phases and boundary layers to have different hardness values. The hardness was greater with NiTi and NiZr, NiZr₂ particles than with NiZr and NiZr₂ particles. The sample with the TiC, Zr mixture had a less monodisperse composition of crystalline phase grains (Fig. 9) that helped to dissipate more uniformly and completely stresses on boundary particles of the ceramic and metallic phases and to distribute evenly the plastic properties in regional structures of NiTi and NiZr crystalline phases in boundary layers. However, these processes were nonuniformly evolved and slower in the sample with the *c*-ZrO₂, Zr mixture because of the various shapes, degree of sintering (Fig. 8d₁), and large sizes of NiZr and NiZr₂ particles (Fig. 9). As a result, nonuniform and broad boundary layers of mullite-β-SiAlON-*c*-ZrO₂ and (Ta,Nb)B,C-(Nb,Ta)C,B-Ni(Nb,Ta) were noticeable and densified and strengthened these layers differently (Fig. 11b - b₂, d - d₂). Expanding microcracks interacted differently with particles and/or local regions of stresses around particles of these phases during different dissipation of stresses on boundary particles of the ceramic and metallic phases, in particular, rapidly in the presence of NiTi and NiZr, NiZr₂ particles and slower in the presence of NiZr and NiZr₂ particles. This determined the various crack resistances of the samples. Propagation of microcracks along a short tortuous path with a small chip around the indentation was noticeable in the sample with the TiC, Zr mixture with developed plastic properties (Fig. 13b₁) that was caused by active interaction of finely disperse particles of NiTi and NiZr, NiZr₂ with local stressed regions along the (Nb,Ta)C,B boundary layer. On the other hand, the microcracks were tortuous because of interaction of shallow point dislocations in the Ni(Nb,Ta) structure and with local stressed regions around ceramic and metallic particles and (Nb,Ta)C,B boundary layers (Fig. 13b₁₋₀). Contact points of regions of ceramic and metallic phases and the (Nb,Ta)C,B boundary layer were densified and strengthened as a result of these processes. The (Nb,Ta)C,B boundary layer slowed the advance of microcracks (Fig. 13b₁₋₁). Linear propagation of microcracks in various directions with much damage around the indentation at 1300°C (Fig. 13b) was observed in this sample. The sample with the *c*-ZrO₂, Zr mixture had much lower crack resistance. Extensive propagation of microcracks along a long linear trajectories and formation of slight damage and small microcracks along the indentation (Fig. 13d₁) related to uneven and incomplete interaction of highly disperse NiZr and NiZr₂ particles with local

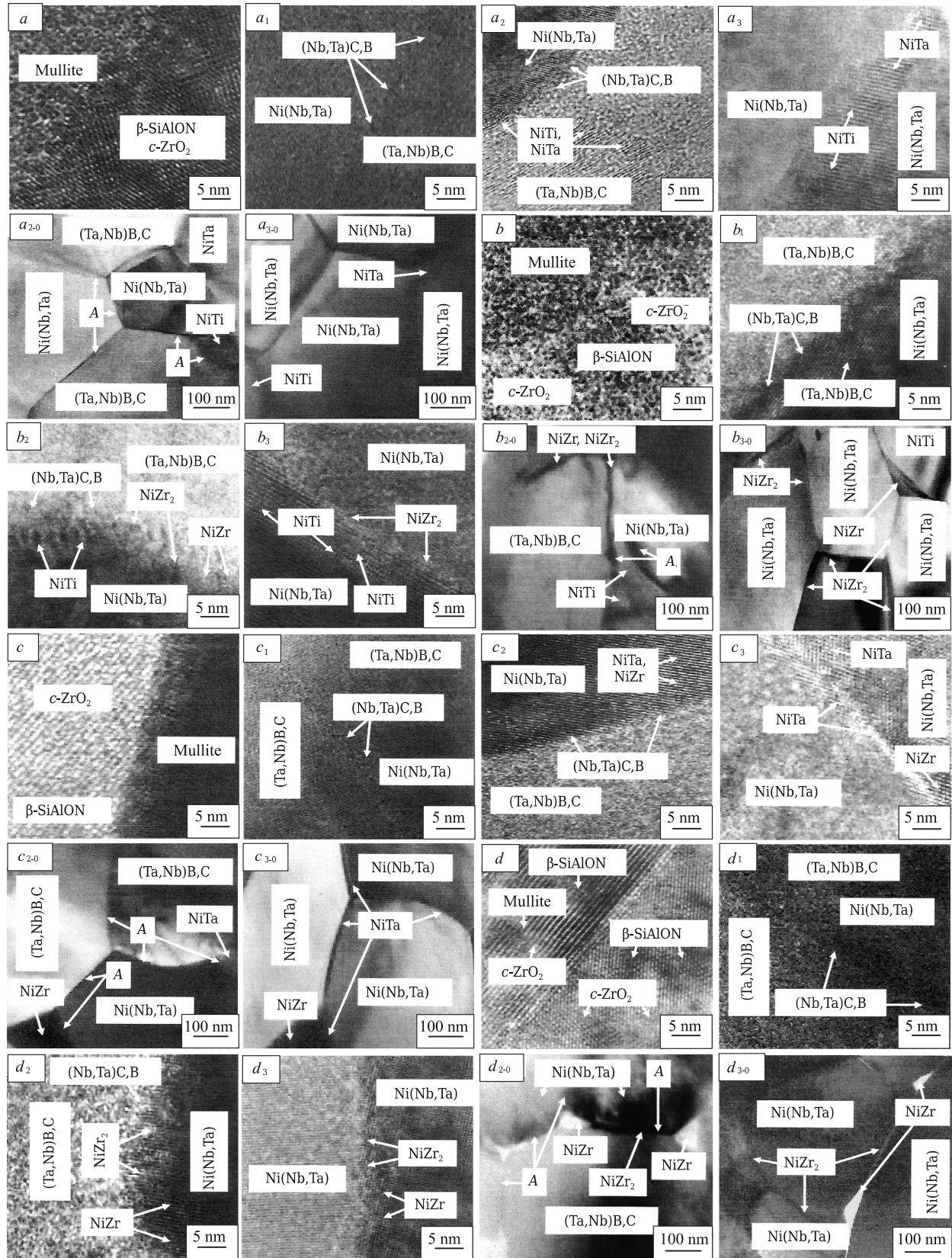


Fig. 11. Microstructure of boundary regions of mullite, β -SiAlON; c -ZrO₂; (Nb,Ta)C,B; (Ta,Nb)B,C; Ni(Nb,Ta); NiTi; NiTa; NiZr; NiZr₂ and grain boundaries of ceramic and metallic phases of M₂₀SiAl₃TiC₂₅Ni₂₅Ta₂₇(50TaB₂-50NbC) ($a - a_3, a_{2-0}, a_{3-0}$), M₂₀SiAl₃TiC₂₅Ni₂₅Zr₂₇(50TaB₂-50NbC) ($b - b_3, b_{2-0}, b_{3-0}$), M₂₀SiAl₃ZrO₂25Ni₂₅Ta₂₇(50TaB₂-50NbC) ($c - c_3, c_{2-0}, c_{3-0}$), and M₂₀SiAl₃ZrO₂25Ni₂₅Zr₂₇(50TaB₂-50NbC) ($d - d_3, d_{2-0}, d_{3-0}$) sintered at 1500°C: *A* is boundary layer (Nb,Ta)C,B.

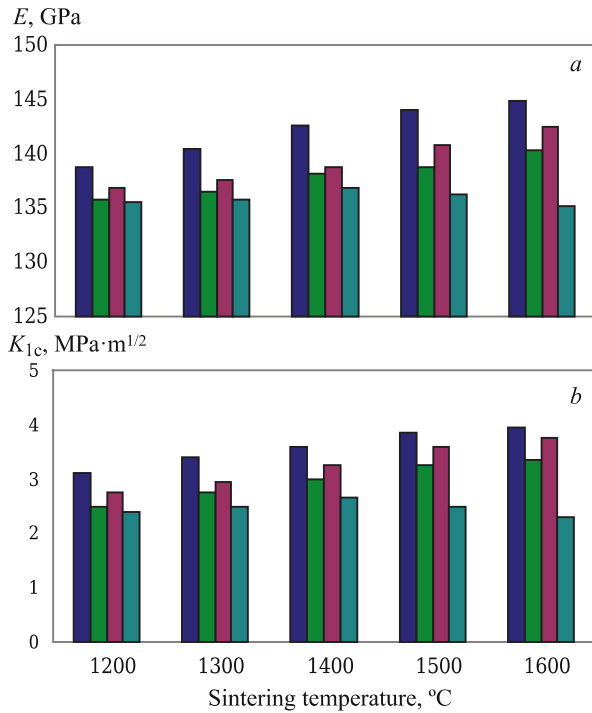


Fig. 12. Change of E (a), K_{1c} (b), and HV (c) of M20SiAl3TiC25Ni25Ta27(50TaB₂-50NbC) (■), M20SiAl3TiC25Ni25Zr27(50TaB₂-50NbC) (■), M20SiAl3ZrO₂25Ni25Ta27(50TaB₂-50NbC) (■), and M20SiAl3ZrO₂25Ni25Zr27(50TaB₂-50NbC) (■) sintered in the range 1200 – 1600°C.

stressed regions along the (Nb,Ta)C,B boundary layer and its embrittlement were observed in it. This was related to the different types of dislocations. In particular, dislocations combined at the boundaries of NiZr, NiZr₂ particles. Dislocations layered at the boundaries of NiZr, NiZr₂,(Nb,Ta)C,B particles (Fig. 13d₁₋₀). Combination of dislocations, in contrast to layering, was associated with great densification and strengthening of the structure, i.e., more developed plastic properties than layered dislocations. As a result, stresses were more evenly dissipated in combined dislocations than in layered dislocations where this process was nonuniform and limited. Thus, plastic properties and hardness evolved more at the boundaries of NiZr, NiZr₂ particles than at boundaries of NiZr, NiZr₂, (Nb,Ta)C,B particles. A narrower short microcrack advanced tortuously through a combined dislocation. A broader microcrack propagated linearly and rapidly through a layered dislocation (Fig. 13d₁₋₁). The crack resistance of the sample with the *c*-ZrO₂, Zr mixture at 1500°C was slighter greater than that of the sample at 1300°C and had much damage and many microcracks around the indentation (Fig. 13d, d₁). The combination of the above processes had different effects on the linear correlation of E and K_{1c} of the samples in the range 1200 – 1600°C (Fig. 14).

The R^2 value differed insignificantly by 0.02 and 0.01 in samples with the Ta, Zr additive. The E and K_{1c} values corre-

lated almost exactly relative to the lines of the samples with the Ta additive in the range 1200 – 1600°C and differed in the range 1500 – 1600°C. As a result, the positions of the lines relative to the E and K_{1c} values differed in the range 1500 – 1600°C as compared to the samples with the Ta additive up to 1500°C. The correlation of the property values was less exact relative to the lines in samples with the Zr additive in the range 1200 – 1600°C, where the property values correlated well for the sample with the TiC, Zr mixture in the range 1200 – 1600°C. However, the position of the lines relative to the E and K_{1c} values of samples with the Zr additive were similar in the range 1200 – 1600°C because the difference of the R^2 values was minimal, indicating a close correlation of the property values relative to each other and positions of lines on the same line of the samples with the Zr additive in the range 1200 – 1600°C.

The correlation of the E and K_{1c} values was about the same relative to the lines of samples with the Ta additive up to 1500°C. This was explained by solid-state diffusion through congruent melting with Ni₃Ti₃ at 1140°C, a peritectic reaction with Ni₈Ta at 1150°C, a eutectic reaction with Ni₈Ta at 1230°C in the sintered composition with the TiC, Ta mixture (Fig. 6a), a peritectic reaction with Ni₇Zr₂, Ni₂₁Zr₈ and Ni₇Zr₂, Ni₅Zr₂ at 1170°C and with Ni₈Ta at 1150°C, a eutectic reaction with Ni₈Ta at 1230°C in the sintered composition with the *c*-ZrO₂/Ta mixture (Fig. 6c), the polydisperse composition of the crystalline phase grains (Fig. 9), and the equal crack resistance (Fig. 13a and c). Differences in the correlation of the property values relative to the lines of samples with the Ta additive in the range 1500 – 1600°C were related to the difference and extent of crystalline phase formation (Fig. 6a and c), the form and degree of sintering (Fig. 8a₁, c₁), the small reduction of polydispersion of crystalline phase grains (Fig. 9), and the difference in the crack resistance (Fig. 13a₁, c₁). These results were responsible for the reduced correlation of the E and K_{1c} values relative to the lines and the small differences of rather high R^2 values of samples with the Ta additive in the range 1200 – 1600°C. This was due to the position of NiTi, NiTa, and NiZr regions of different sizes in the crystal structures of the ceramic and metallic phases; in boundary layers of cermet and metallic phases (Fig. 11a₂, a₃, c₂, c₃) at grain boundaries as thin intermediate layers, separate regions, and grains between them (Fig. 11a₂₋₀, a₃₋₀, c₂₋₀, c₃₋₀) that helped to densify, strengthen, and evolve the plastic properties of boundary layers of mullite-β-SiAlON-*c*-ZrO₂ and (Ta,Nb)B,C-(Nb,Ta)C,B-Ni(Nb,Ta) (Fig. 11a – a₂, c – c₂).

The correlations of the property values relative to the lines of samples with the Zr additive up to 1500°C were similar because of diffusion through congruent melting with Ni₃Ti₃ at 1140°C, a peritectic reaction with Ni₇Zr₃, Ni₂₁Zr₈ and Ni₇Zr₂, Ni₅Zr₂ at 1170°C in the sintered composition with the TiC, Zr mixture (Fig. 6b) and with Ni₇Zr₂, Ni₂₁Zr₈ and Ni₇Zr₂, Ni₅Zr₂ at 1170°C in the sintered composition with the *c*-ZrO₂, Zr mixture (Fig. 6d), the almost equal size distributions of crystalline phase grains (Fig. 9), and the practically identical crack resistance (Fig. 13b and d). Dif-

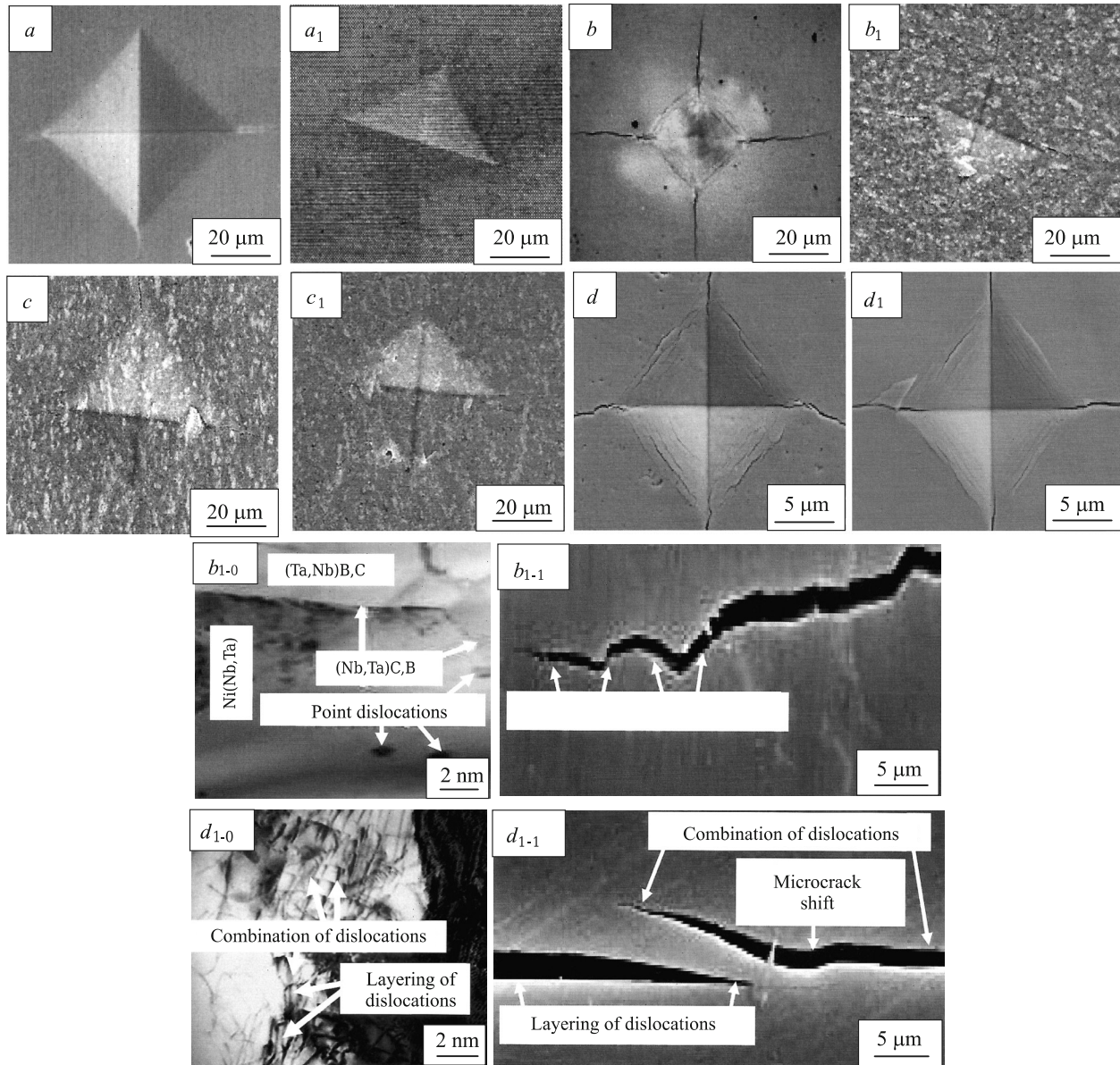


Fig. 13. Photos of indentations for measuring HV of M20SiAl3TiC25Ni25Ta27(50TaB₂–50NbC) (a , a_1), M20SiAl3TiC25Ni25Zr27(50TaB₂–50NbC) (b , b_1), M20SiAl3ZrO₂25Ni25Ta27(50TaB₂–50NbC) (c , c_1), and M20SiAl3ZrO₂25Ni25Zr27(50TaB₂–50NbC) (d , d_1) sintered at 1300 (a – d) and 1600°C (a_1 – d_1) indicating types of dislocations and microcrack propagation trajectories in samples with TiC, Zr (b_{1-0} , b_{1-1}) and c -ZrO₂, Zr mixtures (d_{1-0} , d_{1-1}).

ferences in the correlation of the property values relative to the lines of samples with the Zr additive in the range 1500–1600°C were related to the difference and extent of crystalline phase formation (Fig. 6*b* and *d*), differences in sintering form and degree (Fig. 8*b*₁, *d*₁), the size distribution of crystalline phase grains (Fig. 9), the position of NiTi, NiZr, and NiZr₂ regions at different distances from crystalline boundary layers of ceramic and metallic phases (Fig. 11*b*₂, *b*₃, *d*₂, *d*₃) with intermediate layers of different widths on grain boundaries and separate regions between them (Fig. 11*b*₂₋₀, *b*₃₋₀, *d*₂₋₀, *d*₃₋₀), the significant difference in crack resistance (Fig. 13*b*₁, *d*₁), and the different types of dis-

locations (Fig. 13*b*₁₋₀, *d*₁₋₀) and the different propagation directions of microcracks caused by them (Fig. 13*b*₁₋₁, *d*₁₋₁). These processes and differences in the E and K_{1c} correlations above 1500°C decreased the R^2 values of the samples with the Zr additive in the range 1200–1600°C, where the R^2 value was lowest in the sample with the c -ZrO₂, Zr mixture, in which these processes caused great brittleness and low crack resistance in the boundary layer structures of the crystalline phases and significant destruction of the structure of this sample.

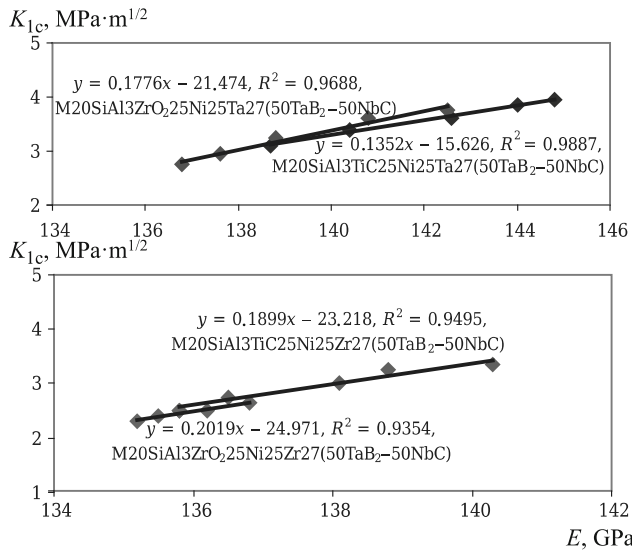


Fig. 14. Linear correlation of E and K_{Ic} of samples in the range 1200 – 1600°C.

CONCLUSION

The effects of Ni, Ta and Ni, Zr powder mixtures in combination with sintered solid solution TaB_2-NbC during spark-plasma sintering of the compositions at a pressing loading of 60 MPa in the range 1200 – 1600°C on the phase composition; percent content of Ti, Ta, and Zr in sialon; the microstructure; the grain sizes of crystalline phases; ρ_{rel} ; Δl ; physical-mechanical properties; and linear correlation of E and K_{Ic} of mullite- β -SiAlON-TiC and mullite- β -SiAlON- c - ZrO_2 samples were shown.

The synthesized powders of β -SiAlON and TiC were characterized by extensive crystallization of β -SiAlON and TiC. c - ZrO_2 spark-plasma sintered at 1400°C and solid solution TaB_2-NbC , at 1800°C, showed extensive crystallization of c - ZrO_2 and (Nb, Ta)C, B phases. The microstructure of solid solution TaB_2-NbC was crystalline, partially nonuniform, and practically completely sintered.

Sintered samples with the Ta, Zr additive showed extensive mullitization; active crystallization of β -SiAlON, (Nb, Ta)C, B, and Ni(Nb, Ta); and varying crystallization of NiTi, NiTa, NiZr, and NiZr₂ in the range 1200 – 1600°C. The microstructure of the ceramic phases with the Ta additive was more evenly and densely sintered with uniform and dense NiTi and NiTa particles, in contrast to the variously densified particles of NiTi, NiZr and NiZr, NiZr₂ in samples with the Zr additive. Sintering of compositions with the Ta additive formed polydisperse compositions of crystalline phase grains and developed uniformly and rapidly. Samples with the Ta additive showed active growth and high physical-mechanical properties, good crack resistance, and a good linear correlation of E and K_{Ic} in the range 1200 – 1600°C.

REFERENCES

1. A. V. Hmelov, "Producing and properties of mullite-sialon- ZrB_2 materials obtained using a spark-plasma technique," *Refract. Ind. Ceram.*, **59**(6), 633 – 641 (2019); *Nov. Ogneupory*, No. 12, 22 – 30 (2018).
2. A. V. Hmelov, "Mullite-TiC- c -BN- c - ZrO_2 materials produced by spark-plasma sintering and their properties," *Refract. Ind. Ceram.*, **60**(1), 86 – 91 (2019); *Nov. Ogneupory*, No. 2, 23 – 29 (2019).
3. A. V. Hmelov, "Development of oxide-free oxide materials under spark-plasma sintering conditions of a mixture of oxide-free components and various metal powder additives," *Refract. Ind. Ceram.*, **61**(1), 73 – 81 (2020); *Nov. Ogneupory*, No. 2, 17 – 25 (2020).
4. R. Vedant, "Development of ZrB_2-B_4C-Mo ceramic matrix composite for high temperature applications," Thesis, National Inst. Technol. Rourkela, 2014, pp. 1 – 61.
5. A. V. Hmelov, "Development of dense materials by plasma-spark sintering of oxide-oxide-free components with different mixtures of metal powders," *Refract. Ind. Ceram.*, **61**(3), 313 – 321 (2020); *Nov. Ogneupory*, No. 6, 27 – 36 (2020).
6. D. Chakravarty and G. Sundararajan, "Microstructure, mechanical properties and machining performance of spark plasma sintered $Al_2O_3-ZrO_2-TiCN$ nanocomposites," *J. Eur. Ceram. Soc.*, **33**(13/14), 2597 – 2607 (2013).
7. A. V. Hmelov, "Preparation of mullite-TiC-ZrC ceramic materials by a plasma-ARC method and their properties," *Refract. Ind. Ceram.*, **57**(6), 645 – 650 (2017); *Nov. Ogneupory*, No. 12, 36 – 41 (2016).
8. A. V. Hmelov, "Strengthening oxide-oxide-free materials by incorporation of TiC-ZrC solid solutions into their structure during spark plasma sintering of initial powder mixtures under high compression load," *Refract. Ind. Ceram.*, **60**(5), 486 – 494 (2020); *Nov. Ogneupory*, No. 10, 18 – 26 (2019).
9. H. Chunfeng, S. Yoshio, and T. Hidehiko, "Microstructure and properties of ZrB_2-SiC composites prepared by spark plasma sintering using $TaSi_2$ as sintering additive," *J. Eur. Ceram. Soc.*, **30**(4), 2625 – 2631 (2010).
10. S. Cardinal, V. Garnier, and G. Fantozzi, "Microstructure and mechanical properties of TiC-TiN based cermets for tool applications," *Int. J. Refract. Met. Hard Mater.*, **27**(2), 521 – 527 (2009).
11. T. Yang, C. Huang, H. Liu, and B. Zou, "Effect of (Ni, Mo) and (W, Ti)C on the microstructure and mechanical properties of TiB_2 ceramic tool materials," *Mater. Sci. Forum*, **723**(4), 233 – 237 (2012).
12. G. Zhang, W. Xiong, Q. Yang, and Z. Yao, "Effect of Mo addition on microstructure and mechanical properties of (Ti, W)C solid solution based cermets," *Int. J. Refract. Met. Hard Mater.*, **43**, 77 – 82 (2014).
13. N. A. Toropov, V. P. Barzakovskii, and R. V. Lapin, *Phase Diagrams of Silicate Systems*, Nauka, (1979), pp. 437 – 439.
14. P. Franke, "Thermodynamic properties of inorganic materials (phase diagram of Ni-Ti) — group IV physical chemistry," *SpringerMaterials*, **19**, Part 4, 1, 2 (2018).
15. A. Nash and P. Nash, "The Ni-Ta (nickel-tantalum) system," *J. Alloy Phase Diagrams*, **5**(3), 259 – 265 (1985).
16. P. Nash and C. S. Jayanth, "The Ni-Zr (nickel-zirconium) system," *J. Alloy Phase Diagrams*, **5**(2), 143 – 146 (1985).
17. F. Predel, "Thermodynamic properties of Ni-Ta (nickel-tantalum) system — phase equilib., crystal. and thermodyn. data of binary all. — physical chemistry," *SpringerMaterials*, **12**, 122, 123 (2016).
18. P. Franke, "Thermodynamic properties of inorganic materials (phase diagram of Ni-Zr) — group IV physical chemistry," *SpringerMaterials*, **19**, Part 4, 1 – 4 (2018).